ACS NANO

www.acsnano.org

ARTICLE

# Nanomolding of Gold and Gold–Silicon Heterostructures at Room Temperature

Arindam Raj, Naijia Liu, Guannan Liu, Sungwoo Sohn, Junxiang Xiang, Ze Liu, and Jan Schroers*

Cite This: https://doi.org/10.1021/acsnano.1c02636

Read Online

ACCESS | Metrics & More | Article Recommendations | Supporting Information

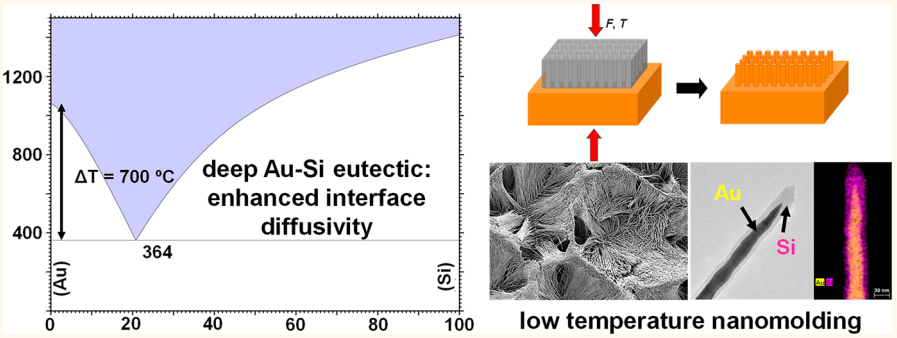


**ABSTRACT:** **Nanofabrication techniques are limited by at least one of the required characteristics such as choice of material, control over geometry, fabrication requirements, yield, cost, and scalability. Our previously developed method of thermomechanical nanomolding fulfills these requirements, although it requires high processing temperatures. Here, we demonstrate low-temperature molding where we utilize the enhanced diffusivity on "eutectic interfaces". Gold nanorods are molded at room temperature using Au–Si alloy as feedstock. Instead of using alloy feedstock, these "eutectic interfaces" can also be established through a feedstock–mold combination. We demonstrate this by using pure Au as feedstock, which is molded into Si molds at room temperature, and also the reverse, Si feedstock is molded into Au molds forming high aspect ratio Au–Si core–shell nanorods. We discuss the mechanism of this low-temperature nanomolding in terms of lower homologous temperature at the eutectic interface. This technique, based on enhanced eutectic interface diffusion, provides a practical nanofabrication method that eliminates the previous high-temperature requirements, thereby expanding the range of the materials that can be practically nanofabricated.**

**KEYWORDS:** *nanofabrication, Au nanorods, Au–Si heterostructures, eutectic systems, interface diffusion*



## INTRODUCTION

The wide spanning technological and research applications of nanomaterials, owing to the engineering control over materials at the nanoscale, require fabrication ability with accurate dimension and shape control on the nanoscale.[1−7] Among the most utilized nanomaterials are gold and silicon, and also their combinations as heterostructures. Gold nanorods are used for a wide range of applications, including plasmonics,[8,9] solar energy harvesting,[10,11] drug delivery,[12,13] biomedical imaging,[14,15] photothermal therapy,[16,17] sensitive chemical detection,[18,19] and metamaterials development.[20,21] The synthesis methods for these nanorods include template-directed synthesis,[22,23] electrochemical growth,[24,25] seed-mediated colloidal growth methods,[26,27] seedless growth,[27,28] photochemical synthesis,[29,30] and mechanical tearing of the nanocrystalline Au film.[31] Wet chemical methods are the most common synthesis processes for gold nanomaterials, where yield and control from seeded growth[32] are usually better than the unseeded ones,[33] but producing the required nanoparticle seeds themselves can be challenging.[34] Generally, producing gold nanoparticles through top-down or bottom-up routes is challenged by either size and shape control or scalability issues.[34]

Enhancing and expanding properties of gold nanoparticles can be achieved by Au–Si hybrid nanostructures. Emergent properties have been argued to originate from the synergistic effects arising from coupling of metal and semiconductor

Received: March 28, 2021
Accepted: August 24, 2021

components.[35,36] For example, the metal component can enhance light absorption of the semiconductor through the localized surface plasmon resonance in photocatalytic applications.[37] Au−Si hybrid nanostructures exhibit better properties compared to pure Au nanorods for localized surface-plasmon resonance applications,[38] localized heating,[39] optical properties,[40] and mechanical properties.[41] In addition, Si-coated Au nanorod arrays are promising candidates for infrared detectors, sensors, subtractive filters and modulators, and hot electron generator applications.[42] Laser ablation[43] and heating Au nanoparticles embedded in a silica matrix above the Au−Si eutectic temperature[38] have been used to synthesize Au−Si nanostructures. Generally, the nanofabrication techniques including those used for gold and silicon are limited in the materials that can be used, and the shapes and sizes that can be realized, each with certain limitations and challenges.[2,44] Nanoimprinting is among the most versatile methods reflected by the wide range of sizes[45] and shapes[46] that can be realized in polymers,[47,48] sol gels such as $SiO_2$, $TiO_2$ gel-based materials[49,50] and amorphous metals,[51,52] and printing over large areas.[53,54] However, it is not suited for crystalline materials, which arguably encompass the majority of the demanded nanomaterials.

A subset of nanomolding, so-called thermomechanical nanomolding (TMNM) (Figure 1a), is promising, as it is suited to fabricate crystalline nanomaterials in a wide range of geometries.[55−58] TMNM can be realized with most metals,[55−57] alloys,[58] and even complex ordered phases such as superconductors, topological insulators, and phase change materials.[58] TMNM is based on atomic diffusion and requires processing temperatures of around $0.5T_m$ ($T_m$: melting temperature in Kelvin) to mold nanowire arrays on the time scale of minutes.[55−57] However, the required high-temperature processing introduces more crystalline defects,[59] results in undesirable reactions with the mold or processing environment,[60] and limits device integration.[61] For example, the requirement of $0.5T_m$ corresponds to 396 °C for gold and 571 °C for silicon. Therefore, it is required to reduce the processing temperature for this processing technique.

Based on the mechanisms for TMNM discussed in the literature,[55,57] a lower processing temperature would drastically reduce nanomoldability, as TMNM is based on diffusion.[57] Drawing on this, we look for systems with appreciably enhanced diffusion at lower temperatures. One example of such systems could be eutectic alloys with their low melting temperatures (such as the Au−Si system in Figure 1b). A drawback in this scheme is that significant solute concentrations are needed to attain deep eutectic compositions, to lower the melting temperature. But we observe that even a minute fraction of solute, *e.g.*, 0.5 at. % of silicon into gold, is sufficient to drastically enhance the nanomoldability. Specifically, when compared to molding at the same temperature of pure Au as feedstock where 1−2 $\mu$m long nanorods can be fabricated in 1 h, with essentially all Au−Si alloy feedstocks with different compositions, nanowires are up to 50 times longer.

This surprising ease of nanofabrication is also demonstrated to be present in other eutectic systems. Hence, this idea can be expanded to a much broader range of materials, many of which are currently unavailable by nanomolding due to the required high processing temperatures. Taking the concept of "eutectic interface" further by creating an artificial "eutectic interface", we use Si as a mold and pure gold as a feedstock material (and *vice versa*). Similar enhancement in nanomolding can be achieved for these Au-moldable material/Si-mold combinations compared to when using a eutectic alloy feedstock.

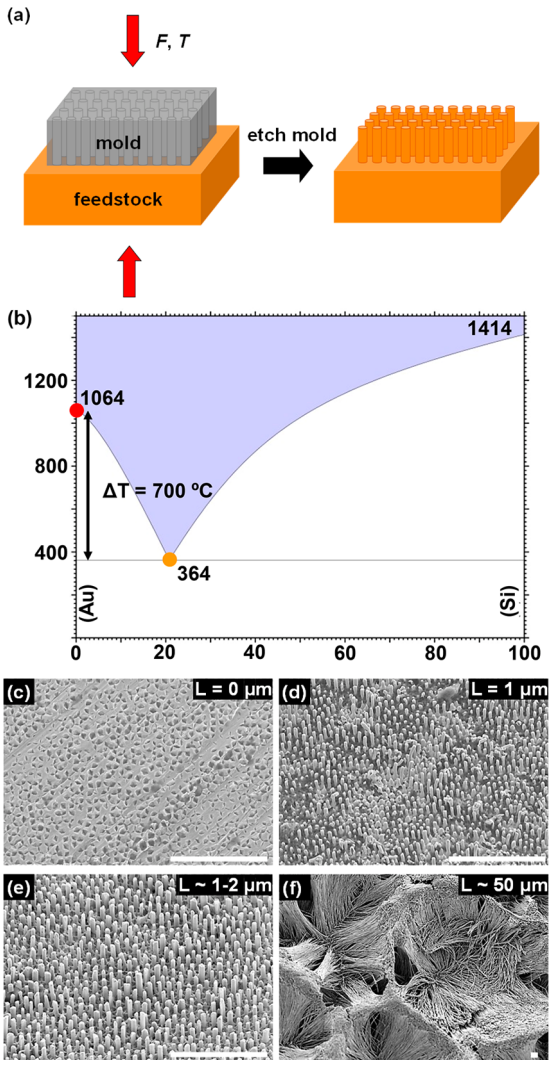


**Figure 1. Enhanced TMNM of Au nanorods with Au and Au−Si feedstocks. (a) Schematic of thermomechanical nanomolding (TMNM), showing a mold (gray) comprising arrays of 250 nm nanocavities in which the feedstock (orange) material such as Au, Si, or Au−Si is pressed at a compressive force, *F*, and temperature, *T*, for a certain time. Etching of the alumina mold dissolves the mold, releasing the nanorod array. (b) Au−Si phase diagram with a deep eutectic, indicating the different feedstock compositions used of 0 and 19 at. % Si (eutectic composition). (c) Using pure gold as feedstock and heating to 30 °C even under a very high stress of 2 GPa applied for 1 h does not result in the formation of nanorods. (d) In contrast, when using $Au_{81}Si_{19}$ as feedstock, nanowires of ~1 $\mu$m in length form, which corresponds to an aspect ratio of ~4; SEM micrograph shown on the right. (e) At 300 °C, the pure Au nanorods have an average growth rate of about 1 $\mu$m/h at 400 MPa. (f) With the eutectic Au−Si feedstock, the growth rate is almost 1 $\mu$m/min at 400 MPa. Scale bars for (c)−(f) measure 5 $\mu$m each.**

## RESULTS AND ANALYSIS

**Low-Temperature Nanomolding for Gold Nanorods.** For TMNM, a compressive force is applied to the mold−


https://doi.org/10.1021/acsnano.1c02636
ACS Nano XXXX, XXX, XXX−XXX

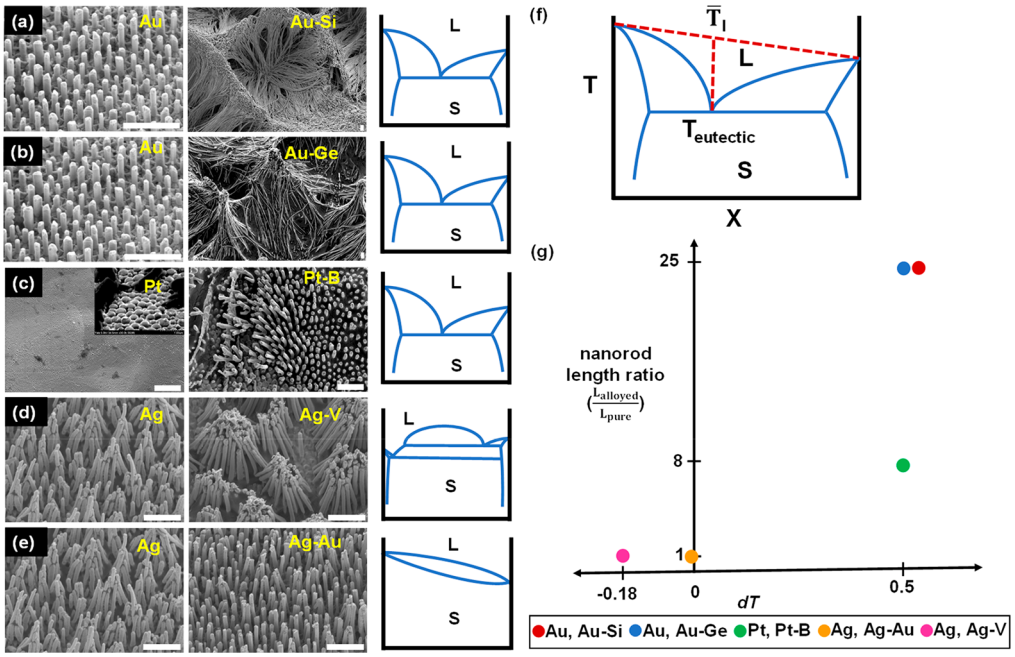


**Figure 2. Correlating enhancement of TMNM with reduction in melting point for different alloys.** (a–e) SEM micrographs showing nanorod arrays for pure metals and alloy systems with various reductions in liquidus temperature for (a) Au and $Au_{81}Si_{19}$, (b) Au and $Au_{95}Ge_5$, (c) Pt and $Pt_{75}B_{25}$, (d) Ag and $Ag_{50}V_{50}$, and (e) Ag and $Au_{50}Ag_{50}$. These micrographs are accompanied by the schematics of their phase diagrams showing a deep eutectic for (a), (b), and (c), a shallow (degenerate) eutectic for (d), and a solid solution for (e). For the deep eutectics, nanorods show the largest increase in length over the pure element. Scale bars for (a)–(e) measure 2 $\mu$m each. (f) To quantify the feature of the eutectic, we introduce $dT = (\overline{T}_l - T_{eutectic})/\overline{T}_l$, where $\overline{T}_l = (X_A T_{m,A} + X_B T_{m,B})$ is a nondimensional indicator of the "depth" of the eutectic, signifying the melting point depression with respect to the linear average. In the case of noneutectic compositions, $T_{eutectic}$ is replaced by $T_{liquidus}$. (g) Measured enhancement of nanomolding ability of the alloy over the pure metal, $\frac{L_{alloyed}}{L_{pure}}$, as a function of d$T$. The eutectic and liquidus temperatures were extracted from the available phase diagrams.[62,64]

feedstock assembly at a fixed temperature, and the atoms from the feedstock move into the mold cavities due to the stress gradient produced by the applied force. Using pure gold as feedstock, heating to 30 °C, and applying a stress of 2 GPa for 1 h on the mold–feedstock assembly with 250 nm nanocavity arrays does not form any nanorods (Figure 1c). In contrast, when using $Au_{81}Si_{19}$ as feedstock, nanowires of ~1 $\mu$m in length, which corresponds to an aspect ratio of ~4, are formed (Figure 1d). When elevating the temperature significantly to 300 °C, nanorods form with a length of ~1–2 $\mu$m from a pure gold feedstock at 400 MPa (Figure 1e). For the same conditions using $Au_{81}Si_{19}$ as feedstock, nanorods of ~50 $\mu$m length are formed (Figure 1f).

Interestingly, on adding Si to Au in the feedstock, the aspect ratio of the nanorods increases by a factor of up to 50, resulting in nanorods as long as 50 $\mu$m. Potentially even longer nanorods can be formed. In the present experiments they are limited by the thickness of the mold, 50 $\mu$m. For the same applied stress, temperature, and mold cavity diameter, the length of the nanorods, $L$, grown through TMNM scales with diffusivity as $L \propto \sqrt{D}$.[57] Our experimental results of different length $L$ when using Au or Au–Si as feedstock allow us to estimate the enhancement in diffusivity when adding Si to Au. Using $\left(\frac{L_{Au-Si}}{L_{Au}}\right)^2 = \left(\frac{D_{Au-Si}}{D_{Au}}\right) \sim 1000$ reveals the dramatic increase by 3 orders of magnitude in the diffusivity of Au atoms in the presence of Si atoms. The obtained nanorods are crystalline, and a discussion on crystallinity of these nanorods is available in the Section S1 of the Supporting Information.

The addition of silicon to gold resulted in significantly longer nanorods due to enhanced diffusion, and the same is expected to be present in other systems with similar deep eutectics in their respective phase diagrams. We hypothesize that in such systems the enhancement in diffusion and, hence, the nanorod length enhancement should scale with an effective lowering of the melting point, which is particularly pronounced in eutectic systems. Such melting point depression is quantified here as $dT = (\overline{T}_l - T_{eutectic})/\overline{T}_l$, where $\overline{T}_l = (X_A T_{m,A} + X_B T_{m,B})$ represents the linear average of the melting points for the constituent elements.

**Enhanced Nanomolding in Other Eutectic Systems.** To test the hypothesis of a scaling of d$T$ with diffusivity and hence nanorod length, we considered a range of alloys with different d$T$ values and performed TMNM at ~0.4$T_m$. This resulted in a similar increase in $L$ for alloys with d$T$ ~ 0.5 such as Au–Ge (5 at. % Ge) and Pt–B (25 at. % B) (Figure 2a–c).[62,63] In systems with d$T$ ~ 0, Au–Ag (50 at. % Au), and d$T$ < 0, Ag–V (40 at. % V), $L$ does not increase in the alloy compared to the pure element (Figure 2d,e). The Ag–V system has a degenerate eutectic (very shallow eutectic, and the eutectic point is located at a small content of Ag/V) on both ends of the phase diagram. Au–Ag features a solid solution (TMNM experimental details for all the considered systems are provided in Table S1 of the Supporting Information). Considering all results of the scaling of d$T$ (Figure 2f) with diffusivity, we argue that the enhancement in


https://doi.org/10.1021/acsnano.1c02636
ACS Nano XXXX, XXX, XXX–XXX

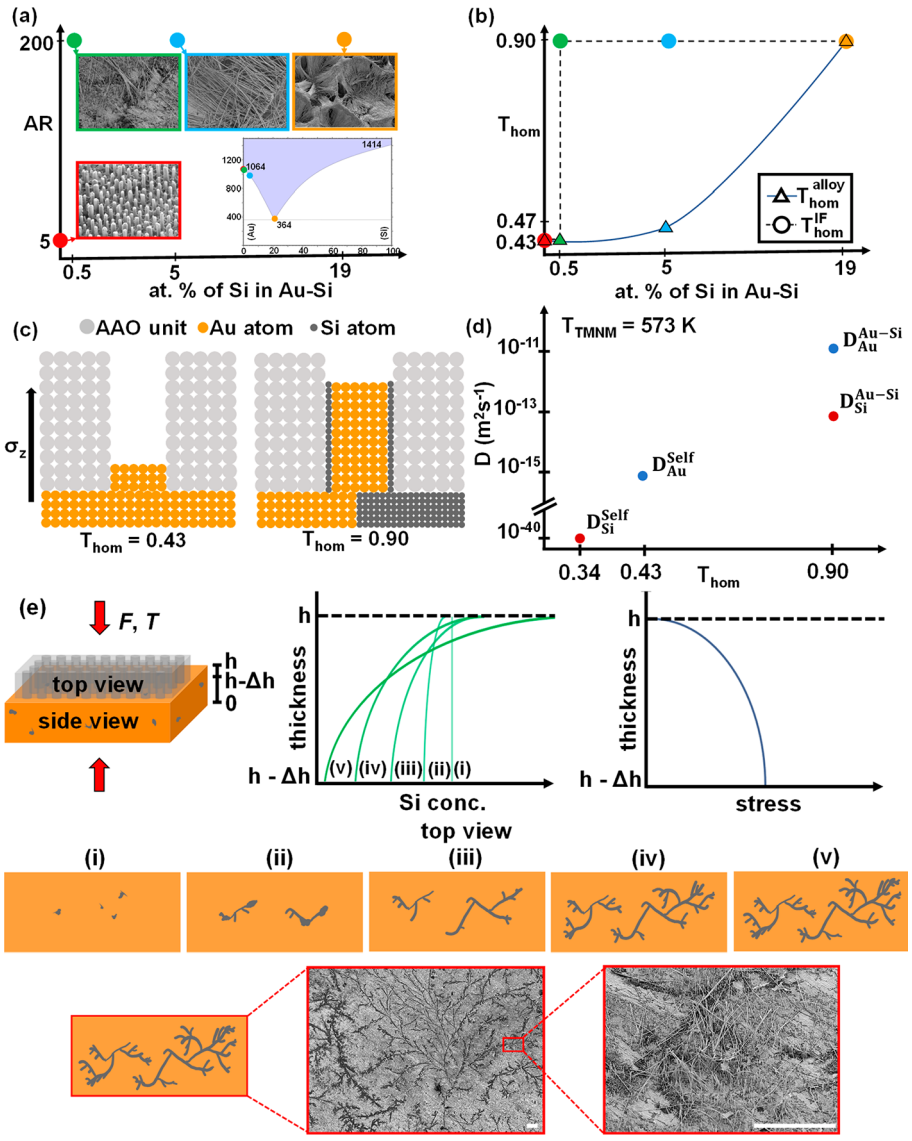


**Figure 3. Mechanism of enhancement of TMNM in a Au−Si alloy and effect of Si concentration on this effect. (a) SEM micrographs of the various alloys molded at 300 °C showing the aspect ratio (AR) of the nanorods formed *vs* the composition of the feedstock alloys. Long nanorods with an AR of 200 are formed for all alloys independent of specific alloy composition. An inset phase diagram of the Au−Si binary system indicates the different alloys used as feedstocks with 0, 0.5, 5, and 19 at. % Si indicated with red, green, blue, and orange dots with $T_m$ = 1064, 1057, 960, and 364 °C, respectively. Scale bars measure 2 $\mu$m each. (b) Graph showing the homologous temperatures for various Au−Si alloy compositions mentioned in (a). Two sets of data are included where the data points represented by filled triangles indicate the homologous temperature calculated from their melting points on the phase diagram, and the circles indicate the homologous temperature at the Au−Si interface. (c) Schematics of the nanomolding process of pure gold and Au−Si alloy. The presence of Si forms Au/Si interfaces where atoms are at a higher Gibbs free energy state and are more loosely packed as compared to their bulk counterparts. As gold forms the deepest eutectic with Si of all elements, the diffusion along the Au/Si interface is enhanced compared to the diffusion on other interfaces, *e.g.*, the Au/AAO interface. Such a Au/Si interface experiences the enhanced $T_{hom}$ of eutectic $Au_{81}Si_{19}$ alloy of 0.90, compared to that of pure gold, $T_{hom}$ = 0.43 at $T_{TMNM}$ = 300 °C. (d) Estimated (from molding experiments) comparison of relative diffusivities of the pure elements in their corresponding phases and in the Au−Si alloy. Diffusivity values were calculated using the equation described in Section S3 of the Supporting Information. The concentration of the Si coating the nanorods is ~5−10%, so it is assumed to be diffusing around 100 times slower compared to Au. Pure Si diffusivity is from extrapolation of self-diffusivity data to low temperatures.[68] (e) Schematics representing the distribution of the Si phase in the Au phase for small Si compositions with the observation of Si fractals and long Au nanorods close to Au/Si interface. The compressive stress drops at the free surfaces over mold cavities at the feedstock/mold interface for a very small thickness, Δ*h*. Si depletes in the bulk and keeps diffusing toward the outer surface in steps (i)−(v). A discussion on stresses generated during TMNM using finite element simulations is presented in Section S4 in the Supporting Information. Top-view schematics for steps (i)−(v) represent snapshots at various instances of this outward diffusion of Si and the formation of Si fractals at the feedstock/mold interface. SEM micrographs show Au nanorods grown on a Au/Si interface only, with Si etched black. Scale bars measure 40 $\mu$m each.**

nanomoldability of an alloy compared to the pure element is reflected in the d$T$ of the alloy system (Figure 2g).

So far, we have shown that nanomoldability (quantified as $L$) in alloys with deep eutectic composition is enhanced over



https://doi.org/10.1021/acsnano.1c02636
ACS Nano XXXX, XXX, XXX−XXX

that of the corresponding pure metals. This finding can be understood by an enhanced homologous temperature, $T_{hom} = \frac{T}{T_m}$ ($T_m$: melting temperature in Kelvin, which becomes the liquidus temperature in an alloy system), in the eutectic alloy, *e.g.*, 364 °C compared to 1068 °C for gold. Hence at 300 °C, $T_{hom}$ for a Au−Si eutectic alloy is 0.90 and 0.43 for Au.

**Significance of the Eutectic Interface for Enhanced Nanomolding.** However, as we will show now, it is not $T_m$ of the considered alloy that matters but rather the lowest accessible melting temperature in the alloy system. This finding is key to understanding the underlying mechanism of the enhanced nanomoldability in eutectic alloy systems. We observed that essentially for all compositions considered here (0.5, 5, 19 at. % Si) the same $L$ is achieved (Figure 3a,b). Even when as little as 0.5 at. % Si is added to gold, the $Au_{99.5}Si_{0.5}$ feedstock with $T_m$ = 1057 °C results in 50 $\mu$m long nanorods. These findings of the composition and $T_m$ dependence of various Au−Si alloys reveal that $L$ is not determined by the melting point of the specific alloy.

Instead, we argue that the nanomoldability of an alloy (quantified as $L$) is determined by the lowest available melting temperature within its alloy system (Figure 3a,b). This suggests that the enhanced nanomoldability during TMNM in Au−Si over Au originates from the presence of an interface where the gold phase and silicon phase come in contact. Such interface is present in alloys containing even as low as 0.5 at. % Si (such low Si concentration would suggest a very small area fraction of interface, which will be discussed later). Hence, in agreement with our experimental finding (Figure 3a,b and Figure 2), nanomoldability (quantified as $\frac{L_{Au-Si}}{L_{Au}}$) is identical to that of the eutectic alloy, even though the melting point of $Au_{99.5}Si_{0.5}$ is 1057 °C and $T_m$ for $Au_{81}Si_{19}$ is 364 °C (Figure 3a,c). We will now discuss the specifics of such an interface, particularly an interface with large d$T$, and why such an interface exhibits enhanced diffusion.

For the Au−Si system, the solubility of Si in the Au phase is significantly less than 0.5 at. % Si; hence, Si precipitates out of the gold phase and Si and Au phases form interfaces (Figure 3c). The properties of the phase interface in eutectic alloys, particularly in Au−Si, have been previously investigated. Weakening of Si−Si bonds in proximity of the Au phase[65] and the presence of nonequilibrium structure/metastable $Au_xSi_y$ species[66,67] have been observed at the interface. This suggests that although Au and Si atoms have strong interactions on the atomic level, the lattice distortion penalty on bulk mixing is too high to allow for any considerable mutual solid-state solubility. But these atomic interactions become important at the interface in a Au−Si alloy which lacks clear crystallographic structure and hence lattice distortion.

In a Au−Si alloy, only the atoms at the Au/Si interface are affected by each other, and these interface atoms are in a thermodynamic environment which is represented by the eutectic temperature on the phase diagram. To clarify, any alloy with composition $Au_xSi_{100-x}$ ($x \neq 0$) heated above $T_{eutectic}$ will melt in part or completely, the latter only if it is exactly at eutectic composition, $Au_{81}Si_{19}$. Hence, the first liquid phase will always appear at the Au/Si interface and will exhibit a eutectic composition of ~$Au_{81}Si_{19}$, irrespective of the composition of the alloy. Thus, in any two-phase Au−Si alloy, the Au/Si interface has the lowest melting point, which is $T_{eutectic}$. These interface atoms experience a higher homologous temperature of $\frac{T}{T_{eutectic}}$ as compared to the Au atoms away from the interface, which experience $T_{hom} = \frac{T}{T_{eutectic}}$. It is this local high homologous temperature that is responsible for the higher diffusion of atoms at the interface (Figure 3c). A brief discussion on the dependence of vacancy-mediated diffusion and homologous temperature for simple systems is shown in Supplementary Section S1 of the Supporting Information.

It is important to note that the diffusion of Au and Si on the Au-phase/Si-phase interface is faster than Au diffusion in the Au phase (Figure 3d). If that would not be the case and $D_{Au}^{self} > D_{Si}^{Au-Si}$, a situation would rapidly occur where there is only Au and no Au/Si interface in the nanomold cavity. Hence, the nanomolding rate would fall back to that of pure gold, *e.g.*, at room temperature to practically zero, in contrast to our observation. For the enhanced nanomoldability both Au and Si atoms are required, and both have to diffuse into the mold cavity. The activation energy for this rapid diffusion of Au during eutectic TMNM with Si is determined to be 137.8 kJ/mol in the 280−340 °C range, lower than the self-diffusion activation enthalpy for Au, 165 kJ/mol[68] (details are presented in Section S3 of the Supporting Information). The amount of Si on the nanowire is very small and segregates to the surface (mold/nanorod interface) due to the immiscibility of Si in the Au phase (Figure 3c). The silicon layer is dissolved through etching, and the resulting nanorods exhibit an indistinct diameter from the mold cavities, suggesting the original thickness of the Si phase on the Au nanorod to be less than a few nanometers. EDS images showing the presence of Si on Au nanorods, where etching was done using phosphoric acid, which leaves the Si layer intact, are shown in the Supporting Information in Section S5.

The difference of the alloy composition and the interface composition (~$Au_{81}Si_{19}$) correlates inversely with the interface volume fraction. For example, in $Au_{99.5}Si_{0.5}$ only a very small volume fraction of atoms is at the eutectic interface configurations. This suggests that the situation where both the Si phase and Au phase are present at the entry of the nanomold cavity (Figure 3c), a requirement for enhanced nanomoldability, is present only for a minute fraction of nanocavities. However, we observed that the Si-rich regions are distributed in a fractal pattern on the surface of the feedstock facing the nanocavity and cover a much larger area than the nominal $Au_{99.5}Si_{0.5}$ composition would suggest (Figure 3e).

Within the alloy feedstock, high stress gradients on the order of $10^{15}$ Pa/m are present. They originate from the applied force, causing a corresponding stress in the feedstock and the boundary condition that stresses vanishing at the free surface of the feedstock above the nanocavities. Such stress gradients cause the Si atoms to diffuse rapidly along the grain boundaries in the bulk feedstock material down the stress gradient toward the mold/feedstock interface. Once these Si atoms reach the interface, they form a fractal-shaped phase, a phenomenon that has been described in metal-induced crystallization studies.[69,70] This causes a higher Si coverage than the nominal alloy composition of the feedstock. The long nanorods, originating from the enhanced nanomold-


https://doi.org/10.1021/acsnano.1c02636
ACS Nano XXXX, XXX, XXX−XXX

ability, grow on the boundaries of these Si-rich phases (Figure 3e). This phenomenon is critical for the hereby proposed method to enhance nanomoldability through eutectic alloying, particularly when very small volume fractions of one constituent are used. Si coverage for a given surface area and correspondingly nanorod growth is maximal around eutectic composition for Au−Si alloys.

In the previously discussed TMNM experiments, we used a "neutral" AAO nanomold. The AAO surface is considered neutral because the interface diffusivity calculated from molding of pure Au in the AAO mold is $\sim 10^{-15}$ $m^2/s$, which is comparable to the grain boundary (GB) diffusivity values of Au at 300 °C of $5.6 \times 10^{-15}$ $m^2/s$.[71] This is considering that the thickness of the feedstock−metal interface where interface diffusion occurs is the same as the GB thickness. So, the AAO mold only acts as a shape-giving and pressure gradient-generating mold but does not contribute to the material transport required for the nanomolding, which predominately occurs on the Au-phase/Si-phase interface. Therefore, we explored replacing the AAO mold/Au−Si alloy feedstock condition with a Si-mold/Au-feedstock or Au-mold/Si-feedstock condition (Figure 4). It has been previously shown that simple mechanical

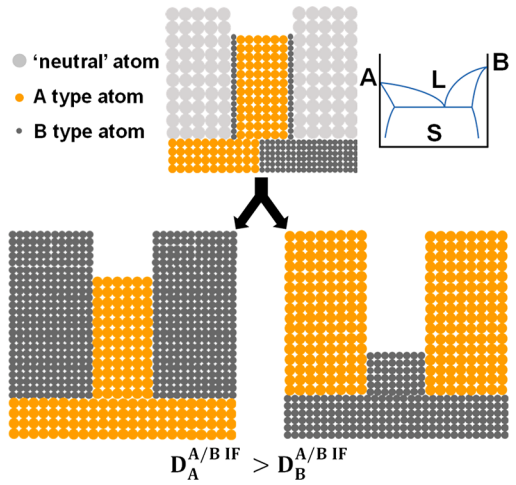


**Figure 4. From a eutectic alloy to mold−feedstock combination. Schematic of translating the rapid diffusion on a A-phase/B-phase eutectic interface into an A-mold/B-feedstock or B-mold/A-feedstock combination. Here, A is assumed to be the faster diffuser at the same homologous temperature at the A/B interface than B, resulting in longer B nanorods.**

contact of pure Au and Si bulk crystals above the eutectic temperature results in melting,[72,73] where the contacting interface appears to capture aspects of eutectic behavior (another supporting experiment showing easy nanomolding of gold just due to mechanical contact with Si is shown in Supplementary Section S6 of the Supporting Information). Here, we seek to explore if the fast diffusion characteristics below the eutectic point can also be explored through creating an artificial eutectic interface through Si-mold/Au-feedstock or Au-mold/Si-feedstock.

**Mold−Feedstock Combination from Eutectic Pairs.** Using pure gold as feedstock and silicon as a mold material, several microns long Au nanowires are molded under an applied compressive stress of 2 GPa at 30 °C for 1 h (Figure 5a,b). In contrast, under the same conditions, nanomolding

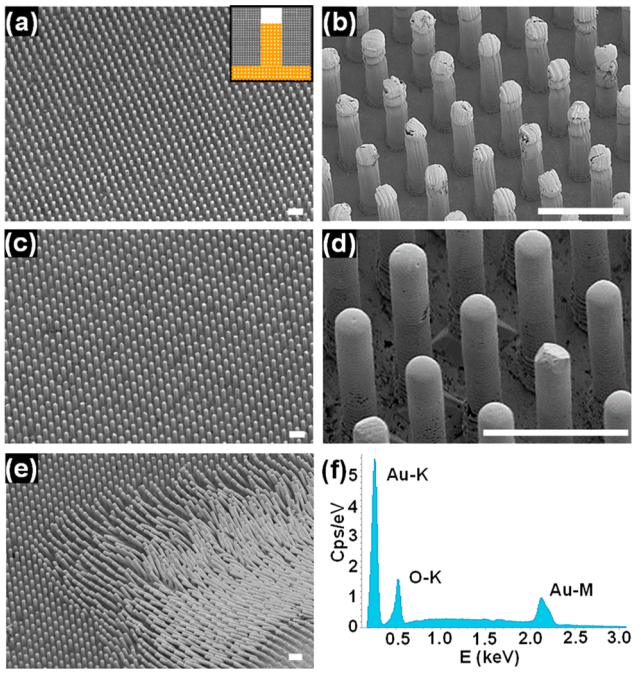


**Figure 5. Enhanced TMNM of Au into Si nanomolds. (a) SEM micrograph of Au nanorods formed in a Si mold at 30 °C. (b) Zoomed-in micrograph showing the surface of Au nanorods shown in (a). (c) SEM micrograph of Au nanorods formed in a Si mold at 300 °C. (d) Zoomed-in micrograph revealing the surface of Au nanorods shown in (c). (e) Some of the Au rods in (a) deformed to show their attachment to the substrate. Scale bars for (a)−(e) measure 5 μm each. (f) EDS analysis reveals the composition of the nanorods to be pure Au (no Si peaks observed).**

pure gold using an AAO mold is not possible (Figure 1c). The behavior of enhanced nanomoldability when using silicon as a mold instead of AAO is present at enhanced temperatures, also shown for 300 °C, even at lower stresses of 400 MPa (Figure 5c−e). EDS data confirm that the nanorods obtained after etching away the Si mold are essentially pure gold (Figure 5f). Annealing after molding can help smoothen the rough profile of the nanorods; a brief discussion is provided in Supplementary Section S7 of the Supporting Information. A discussion on the possible effects of oxidation of the Si mold on this TMNM processing is also provided in Supplementary Section S8 of the Supporting Information.

We also considered the reversed order, where we use a Au mold and Si feedstock. For experimental convenience, we fabricated Au molds by sputtering a ~250 nm Au layer on and into AAO nanomolds. We used a pure crystalline silicon wafer as feedstock, which was pressed at 300 °C with ~400 MPa for 60 min into the 250 nm Au/mold nanocavities (Figure 6a). This resulted in very long nanowires. To date, direct nanomolding of silicon is not possible despite its technological importance.[58] Micrographs for the Au sputtered AAO mold and cross sections for Si molds are provided in the Supporting Information in Supplementary Section S9.

However, these molded nanorods are not pure silicon but exhibit a core−shell structure as revealed through TEM imaging (Figure 6b). We argue that the origin for the core−shell structure comprising silicon and gold originates predominately from the faster diffusion of gold than Si in


https://doi.org/10.1021/acsnano.1c02636
ACS Nano XXXX, XXX, XXX−XXX

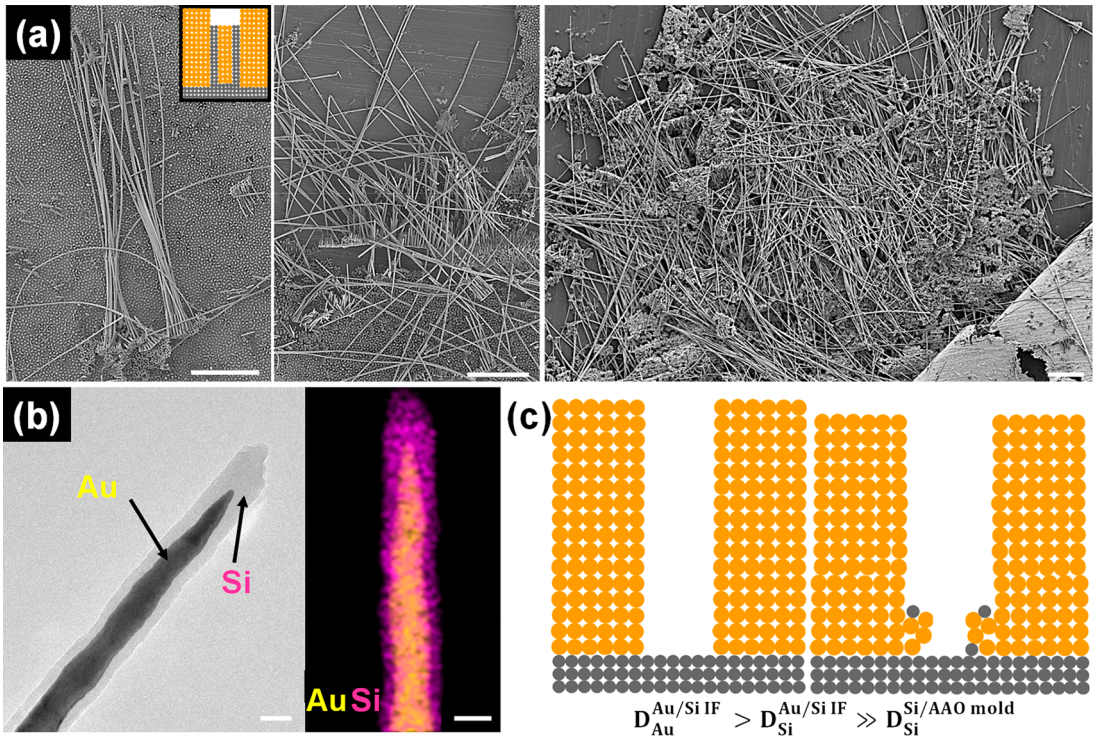


**Figure 6. Enhanced TMNM of the Si feedstock into Au nanomolds. (a) SEM micrograph showing nanorods of 250 nm in diameter obtained from pressing Si on a Au mold (prepared by sputtering a 250 nm film on top of AAO nanomold). During etching, the nanorods tend to clump together due to their high aspect ratio and often detach from the substrate. Scale bars measure 10 $\mu$m each. (b) TEM image showing elemental distribution in one such wire, here pressed in a 40 nm diameter mold for ease of TEM imaging, showing a Si capsule around the Au core. Scale bars measure 30 nm each. (c) Schematic explaining the formation of the Au−Si core−shell. The high stresses deform the Au mold, causing the Au atoms to experience the pressure gradient and diffuse in addition to the Si atoms from the feedstock.**

Au−Si (see Figure 3d). Under ideal conditions the mold would not deform, and the mold walls are parallel to the applied force and, hence, no driving force for diffusion down the pressure gradient exists. In that case the formation of pure Si nanorods in Au molds should occur despite the much higher diffusivity of Au than Si in Au−Si. However, the gold mold, as it is significantly softer than silicon, deforms and the mold walls deform and experience a finite stress gradient (Figure 6c). This, finite, likely very small gradient, $\Delta\sigma$, will enable gold diffusion down into the nanocavity. The material flux, $dL/dt$, is proportional to $\Delta\sigma \times D$. The ratio of the Au phase and Si phase in the core−shell nanowire is given by the ratio $\left(\frac{\Delta\sigma \times D_{Au}^{Au/Si\ IF}}{\Delta\sigma \times D_{Si}^{Au/Si\ IF}}\right)$, where $D_x^{Au/Si\ IF}$ is the diffusivity of $x$ atom (Au or Si) on the Au/Si interface. Hence, only if deformation of the mold can be avoided could a pure silicon rod be formed. The opposite scenario, using Si-mold/Au-feedstock to nanomold gold at room temperature, due to the high strength of silicon as compared to gold, is of course easier to establish experimentally.

## CONCLUSION

In conclusion, we show that eutectic mixtures with a low melting point may be nanomolded at very low temperatures. This ease of nanomolding is correlated with the effective lowering of the melting point in the alloy system due to the presence of a eutectic point. The enhanced nanomolding is enabled by the eutectic interface and, hence, is not a function of the alloy composition, but defined by the lowest available melting temperature in the alloy system. This finding, suggesting that only traces of one element are needed to enhance molding of another element, occurs due to rapid diffusion on the eutectic interface that behaves like a eutectic system with a lower melting temperature. This situation can also be realized when a mold made of one material from a low-melting eutectic is used for low-temperature TMNM of another material, *e.g.*, a Au mold for Si or *vice versa*. We expect that further exploration of such enhanced nanomolding will expand nanofabrication to include elements that have been previously elusive due to their challenging processing requirements.

## METHODS

**Alloy Preparation.** Alloys were prepared using pure constituent elements molten and mixed together in an arc melting furnace in an inert Argon environment.

**Molding.** For our TMNM experiments, the feedstock material was pressed at a compressive stress for a certain duration, with the mold between two heated plates on an Instron Universal testing machine. The molding is isothermal under a constant load, where the load is applied over a period of 10 min, and then held for a fixed period of time. This was followed by etching of the mold using a 3 M KOH aqueous solution or a 20% v/v $H_3PO_4$ aqueous solution to release the molded nanowires. The details for different materials and molding parameters are provided in Supplementary Table S1. Three types of molds (Si, plain anodic alumina, and gold-sputtered anodic alumina) were used in this work. Si-based molds were fabricated by conventional photolithographic and etching techniques. Commercially available nanoporous alumina was used as a template for


https://doi.org/10.1021/acsnano.1c02636
ACS Nano XXXX, XXX, XXX−XXX

nanomolding. These were sputtered to coat their top layer with 250 nm Au film to form the gold-coated nanomolds.

## ASSOCIATED CONTENT

### Supporting Information

The Supporting Information is available free of charge at https://pubs.acs.org/doi/10.1021/acsnano.1c02636.

Table S1: TMNM conditions for the samples; supplementary sections on crystallinity of Au nanorods; homologous temperature and diffusion term correlation; activation energy of Au during eutectic TMNM including Table S2; finite element analysis of feedstock deformation during TMNM; EDS of long Au−Si nanorods; fast nanomolding of Au only requiring mechanical contact with Si; effect of annealing Au nanorods; TMNM processing in air; description of the molds; Figures S1−S7; supplementary references (PDF)

## AUTHOR INFORMATION


### Corresponding Author

**Jan Schroers** − *Department of Mechanical Engineering and Materials Science, Yale University, New Haven, Connecticut 06511, United States*; Email: jan.schroers@yale.edu

### Authors

**Arindam Raj** − *Department of Mechanical Engineering and Materials Science, Yale University, New Haven, Connecticut 06511, United States*; orcid.org/0000-0001-7277-6770

**Naijia Liu** − *Department of Mechanical Engineering and Materials Science, Yale University, New Haven, Connecticut 06511, United States*

**Guannan Liu** − *Department of Mechanical Engineering and Materials Science, Yale University, New Haven, Connecticut 06511, United States*

**Sungwoo Sohn** − *Department of Mechanical Engineering and Materials Science, Yale University, New Haven, Connecticut 06511, United States*

**Junxiang Xiang** − *Department of Engineering Mechanics, School of Civil Engineering, Wuhan University, 430072 Wuhan, People's Republic of China*

**Ze Liu** − *Department of Engineering Mechanics, School of Civil Engineering, Wuhan University, 430072 Wuhan, People's Republic of China*; orcid.org/0000-0002-9906-5351

Complete contact information is available at: https://pubs.acs.org/10.1021/acsnano.1c02636


### Author Contributions

A.R. and J.S. designed and developed the study. A.R., N.L., and G.L. conducted the sample preparation, molding, and SEM characterization experiments. S.S. conducted the TEM characterization. J.X. and Z.L. worked on the FEA simulations for the TMNM process. A.R. and J.S. analyzed the data and wrote the manuscript. All authors contributed to the discussion of the results. The manuscript was written through contributions of all authors. All authors have given approval to the final version of the manuscript.

### Notes

The authors declare no competing financial interest.

## ACKNOWLEDGMENTS

We warmly thank Dr. Jittisa Ketkaew for their help with silicon mold fabrication. This work was supported by the National Science Foundation through the Advanced Manufacturing Program (CMMI 1901613).

## REFERENCES


(1) Xia, Y. N.; Lim, B. Nanotechnology: Beyond the Confines of Templates. *Nature* **2010**, *467*, 923−924.

(2) Liddle, J. A.; Gallatin, G. M. Nanomanufacturing: A Perspective. *ACS Nano* **2016**, *10*, 2995−3014.

(3) Tawfick, S.; De Volder, M.; Copic, D.; Park, S. J.; Oliver, C. R.; Polsen, E. S.; Roberts, M. J.; Hart, A. J. Engineering of Micro- and Nanostructured Surfaces with Anisotropic Geometries and Properties. *Adv. Mater.* **2012**, *24*, 1628−1674.

(4) Xie, D. G.; Nie, Z. Y.; Shinzato, S.; Yang, Y. Q.; Liu, F. X.; Ogata, S.; Li, J.; Ma, E.; Shan, Z. W. Controlled Growth of Single-Crystalline Metal Nanowires *via* Thermomigration across a Nanoscale Junction. *Nat. Commun.* **2019**, *10*, 4478.

(5) Richter, G.; Hillerich, K.; Gianola, D. S.; Monig, R.; Kraft, O.; Volkert, C. A. Ultrahigh Strength Single Crystalline Nanowhiskers Grown by Physical Vapor Deposition. *Nano Lett.* **2009**, *9*, 3048−3052.

(6) Yoon, G.; Kim, I.; Rho, J. Challenges in Fabrication towards Realization of Practical Metamaterials. *Microelectron. Eng.* **2016**, *163*, 7−20.

(7) Oh, D. K.; Jeong, H.; Kim, J.; Kim, Y.; Kim, I.; Ok, J. G.; Rho, J. Top-Down Nanofabrication Approaches toward Single-Digit-Nanometer Scale Structures. *J. Mech. Sci. Technol.* **2021**, *35*, 837−859.

(8) Chen, H. J.; Shao, L.; Li, Q.; Wang, J. F. Gold Nanorods and Their Plasmonic Properties. *Chem. Soc. Rev.* **2013**, *42*, 2679−2724.

(9) Tian, L. M.; Chen, E.; Gandra, N.; Abbas, A.; Singamaneni, S. Gold Nanorods as Plasmonic Nanotransducers: Distance-Dependent Refractive Index Sensitivity. *Langmuir* **2012**, *28*, 17435−17442.

(10) Chang, S.; Li, Q.; Xiao, X. D.; Wong, K. Y.; Chen, T. Enhancement of Low Energy Sunlight Harvesting in Dye-Sensitized Solar Cells Using Plasmonic Gold Nanorods. *Energy Environ. Sci.* **2012**, *5*, 9444−9448.

(11) Zheng, Y. Z.; Tao, X.; Zhang, J. W.; Lai, X. S.; Li, N. Plasmonic Enhancement of Light-harvesting Efficiency in Tandem Dye-Sensitized Solar Cells Using Multiplexed Gold Core/Silica Shell Nanorods. *J. Power Sources* **2018**, *376*, 26−32.

(12) Park, H.; Yang, S.; Kang, J. Y.; Park, M. H. On-Demand Drug Delivery System Using Micro-Organogels with Gold Nanorods. *ACS Med. Chem. Lett.* **2016**, *7*, 1087−1091.

(13) Wei, X.; Mazid, R.; Yap, L. W.; Li, X. Y.; Cheng, W. L. Plasmonic Caged Gold Nanorods for Near-Infrared Light Controlled Drug Delivery. *Nanoscale* **2014**, *6*, 14388−14393.

(14) Ma, Z. F.; Tian, L.; Di, J.; Ding, T. Bio-Detection, Cellular Imaging and Cancer Photothermal Therapy Based on Gold Nanorods. *Prog. Chem.* **2009**, *21*, 134−142.

(15) Huang, X. H.; Neretina, S.; El-Sayed, M. A. Gold Nanorods: From Synthesis and Properties to Biological and Biomedical Applications. *Adv. Mater.* **2009**, *21*, 4880−4910.

(16) Wu, Y.; Ali, M. R. K.; Dong, B.; Han, T. G.; Chen, K. C.; Chen, J.; Tang, Y.; Fang, N.; Wang, F. J.; El-Sayed, M. A. Gold Nanorod Photothermal Therapy Alters Cell Junctions and Actin Network in Inhibiting Cancer Cell Collective Migration. *ACS Nano* **2018**, *12*, 9279−9290.

(17) Fourkal, E.; Veltchev, I.; Tafo, A. G.; Ma, C.; Khazak, V.; Skobeleva, N. Photo-Thermal Cancer Therapy Using Gold Nanorods. In *International Federation for Medical and Biological Engineering (IFMBE) Proceedings, Proceedings of the World Congress on Medical Physics and Biomedical Engineering*, Munich, Germany, September 7−12, 2009; Dössel, O.; Schlegel, W. C., Eds.; Springer: Berlin, Heidelberg, 2009; Vol 25/7, pp 761−763.

(18) Nie, S. M.; Emery, S. R. Probing Single Molecules and Single Nanoparticles by Surface-Enhanced Raman Scattering. *Science* **1997**, *275*, 1102−1106.
(19) Kim, D.; Choi, E.; Lee, C.; Choi, Y.; Kim, H.; Yu, T.; Piao, Y. Highly Sensitive and Selective Visual Detection of CR(VI) Ions Based on Etching of Silver-Coated Gold Nanorods. *Nano Converg* **2019**, *6*, 34.
(20) Morgan, F.; Murphy, A.; Hendren, W.; Wurtz, G.; Pollard, R. J. *In Situ* Ellipsometric Monitoring of Gold Nanorod Metamaterials Growth. *ACS Appl. Mater. Interfaces* **2017**, *9*, 17380−17387.
(21) Chandrasekar, R.; Wang, Z. X.; Meng, X. G.; Azzam, S. I.; Shalaginov, M. Y.; Lagutchev, A.; Kim, Y. L.; Wei, A.; Kildishev, A. V.; Boltasseva, A.; Shalaev, v. M. Lasing Action with Gold Nanorod Hyperbolic Metamaterials. *ACS Photonics* **2017**, *4*, 674−680.
(22) Sun, Y.; Xia, Y. Shape-Controlled Synthesis of Gold and Silver Nanoparticles. *Science* **2002**, *298*, 2176−2179.
(23) Nakamura, S.; Mitomo, H.; Sekizawa, Y.; Higuchi, T.; Matsuo, Y.; Jinnai, H.; Ijiro, K. Strategy for Finely Aligned Gold Nanorod Arrays Using Polymer Brushes as a Template. *Langmuir* **2020**, *36*, 3590−3599.
(24) Chang, S. S.; Shih, C. W.; Chen, C. D.; Lai, W. C.; Wang, C. R. C. The Shape Transition of Gold Nanorods. *Langmuir* **1999**, *15*, 701−709.
(25) Abdelmoti, L. G.; Zamborini, F. P. Potential-Controlled Electrochemical Seed-Mediated Growth of Gold Nanorods Directly on Electrode Surfaces. *Langmuir* **2010**, *26*, 13511−13521.
(26) Jana, N. R.; Gearheart, L.; Murphy, C. J. Wet Chemical Synthesis of High Aspect Ratio Cylindrical Gold Nanorods. *J. Phys. Chem. B* **2001**, *105*, 4065−4067.
(27) Requejo, K. I.; Liopo, A. V.; Zubarev, E. R. Gold Nanorod Synthesis with Small Thiolated Molecules. *Langmuir* **2020**, *36*, 3758−3769.
(28) Xu, X. L.; Zhao, Y. Y.; Xue, X. D.; Huo, S. D.; Chen, F.; Zou, G. Z.; Liang, X. J. Seedless Synthesis of High Aspect Ratio Gold Nanorods with High Yield. *J. Mater. Chem. A* **2014**, *2*, 3528−3535.
(29) Kim, F.; Song, J. H.; Yang, P. D. Photochemical Synthesis of Gold Nanorods. *J. Am. Chem. Soc.* **2002**, *124*, 14316−14317.
(30) Ahmed, M.; Narain, R. Rapid Synthesis of Gold Nanorods Using a One-Step Photochemical Strategy. *Langmuir* **2010**, *26*, 18392−18399.
(31) Liu, P.; Wang, L. H.; Yue, Y. H.; Song, S. X.; Wang, X. D.; Reddy, K. M.; Liao, X. Z.; Zhang, Z.; Chen, M. W.; Han, X. D. Room-Temperature Superplasticity in Au Nanowires and Their Atomistic Mechanisms. *Nanoscale* **2019**, *11*, 8727−8735.
(32) Lei, Y.; Cai, W. P.; Wilde, G. Highly Ordered Nanostructures with Tunable Size, Shape and Properties: A New Way to Surface Nano-Patterning Using Ultra-Thin Alumina Masks. *Prog. Mater. Sci.* **2007**, *52*, 465−539.
(33) Scarabelli, L.; Sanchez-Iglesias, A.; Perez-Juste, J.; Liz-Marzan, L. M. A "Tips and Tricks" Practical Guide to the Synthesis of Gold Nanorods. *J. Phys. Chem. Lett.* **2015**, *6*, 4270−4279.
(34) De Oliveira, P. F. M.; Torresi, R. M.; Emmerling, F.; Camargo, P. H. C. Challenges and Opportunities in the Bottom-up Mechanochemical Synthesis of Noble Metal Nanoparticles. *J. Mater. Chem. A* **2020**, *8*, 16114−16141.
(35) Volokh, M.; Mokari, T. Metal/Semiconductor Interfaces in Nanoscale Objects: Synthesis, Emerging Properties and Applications of Hybrid Nanostructures. *Nanoscale Adv.* **2020**, *2*, 930−961.
(36) Lv, Y. P.; Duan, S. B.; Wang, R. M. Structure Design, Controllable Synthesis, and Application of Metal-Semiconductor Heterostructure Nanoparticles. *Prog. Nat. Sci.* **2020**, *30*, 1−12.
(37) Jiang, R.; Li, B.; Fang, C.; Wang, J. Metal/Semiconductor Hybrid Nanostructures for Plasmon-Enhanced Applications. *Adv. Mater.* **2014**, *26*, 5274−309.
(38) Mohapatra, S.; Mishra, Y. K.; Avasthi, D. K.; Kabiraj, D.; Ghatak, J.; Varma, S. Synthesis of Gold-Silicon Core-Shell Nanoparticles with Tunable Localized Surface Plasmon Resonance. *Appl. Phys. Lett.* **2008**, *92*, 103105.
(39) Zograf, G. P.; Petrov, M. I.; Makarov, S. V. Coating of Au Nanoparticle by Si Shell for Enhanced Local Heating. *J. Phys.: Conf. Ser.* **2017**, *929*, 012072.
(40) Zograf, G. P.; Rybin, M. V.; Zuev, D. A.; Makarov, S. V.; Below, P. A.; Lopanitsyna, N. Y.; Kuksin, A. Y.; Starikov, S. V. Modeling of Formation Mechanism and Optical Properties of Si/Au Core-Shell Nanoparticles. In *2016 Days on Diffraction, Proceedings of the International Conference on Days on Diffraction*; St. Petersburg, Russia, June 27−July 1, 2016; Motygin, O. V.; Kiselev, A. P.; Kapitanova, P. V.; Goray, L. I.; Kazakov, A. Ya.; Kirpichnikova, A. S., Eds.; IEEE Publishing: Piscataway, NJ, USA, 2016; pp 460−463.
(41) Guillotte, M.; Godet, J.; Pizzagalli, L. Molecular Dynamics Study of Mechanical Behavior of Gold-Silicon Core-Shell Nanowires under Cyclic Loading. *Materialia* **2019**, *5*, 100204.
(42) Zhou, J.; Liu, Z.; Liu, X.; Pan, P.; Zhan, X.; Liu, Z. Silicon-Au Nanowire Resonators for High-Q Multiband Near-Infrared Wave Absorption. *Nanotechnology* **2020**, *31*, 375201.
(43) Nasiri, P.; Doranian, D.; Sari, A. H. Synthesis of Au/Si Nanocomposite Using Laser Ablation Method. *Opt. Laser Technol.* **2019**, *113*, 217−224.
(44) Gates, B. D.; Xu, Q. B.; Stewart, M.; Ryan, D.; Willson, C. G.; Whitesides, G. M. New Approaches to Nanofabrication: Molding, Printing, and Other Techniques. *Chem. Rev.* **2005**, *105*, 1171−1196.
(45) Li, R.; Chen, Z.; Datye, A.; Simon, G. H.; Ketkaew, J.; Kinser, E.; Liu, Z.; Zhou, C.; Dagdeviren, O. E.; Sohn, S.; Singer, J. P.; Osuji, C. O.; Schroers, J.; Schwarz, U. D. Atomic Imprinting into Metallic Glasses. *Commun. Phys.* **2018**, *1*, 75.
(46) Hasan, M.; Schroers, J.; Kumar, G. Functionalization of Metallic Glasses through Hierarchical Patterning. *Nano Lett.* **2015**, *15*, 963−968.
(47) Chou, S. Y.; Krauss, P. R.; Renstrom, P. J. Nanoimprint Lithography. *J. Vac. Sci. Technol., B: Microelectron. Process. Phenom.* **1996**, *14*, 4129−4133.
(48) Tan, H.; Gilbertson, A.; Chou, S. Y. Roller Nanoimprint Lithography. *J. Vac. Sci. Technol., B: Microelectron. Process. Phenom.* **1998**, *16*, 3926−3928.
(49) Li, L.; Zhang, P.; Wang, W. M.; Lin, H. T.; Zerdoum, A. B.; Geiger, S. J.; Liu, Y. C.; Xiao, N.; Zou, Y.; Ogbuu, O.; Du, Q. Y.; Jia, X. Q.; Li, J. J.; Hu, J. J. Foldable and Cytocompatible Sol-Gel $TiO_2$ Photonics. *Sci. Rep.* **2015**, *5*, 13832.
(50) Yoon, G.; Kim, K.; Huh, D.; Lee, H.; Rho, J. Single-Step Manufacturing of Hierarchical Dielectric Metalens in the Visible. *Nat. Commun.* **2020**, *11*, 2268.
(51) Kumar, G.; Tang, H. X.; Schroers, J. Nanomoulding with Amorphous Metals. *Nature* **2009**, *457*, 868−872.
(52) Liu, Z.; Schroers, J. General Nanomoulding with Bulk Metallic Glasses. *Nanotechnology* **2015**, *26*, 145301.
(53) Wang, C.; Xia, Q. F.; Li, W. D.; Fu, Z. L.; Morton, K. J.; Chou, S. Y. Fabrication of a 60-nm-Diameter Perfectly Round Metal-Dot Array Over a Large Area on a Plastic Substrate Using Nanoimprint Lithography and Self-Perfection by Liquefaction. *Small* **2010**, *6*, 1242−1247.
(54) Kooy, N.; Mohamed, K.; Pin, L. T.; Guan, O. S. A Review of Roll-to-Roll Nanoimprint Lithography. *Nanoscale Res. Lett.* **2014**, *9*, 320.
(55) Liu, Z. One-Step Fabrication of Crystalline Metal Nanostructures by Direct Nanoimprinting below Melting Temperatures. *Nat. Commun.* **2017**, *8*, 14910.
(56) Liu, Z.; Han, G.; Sohn, S.; Liu, N.; Schroers, J. Nanomolding of Crystalline Metals: The Smaller the Easier. *Phys. Rev. Lett.* **2019**, *122*, 036101.
(57) Liu, Z. Investigation of Temperature and Feature Size Effects on Deformation of Metals by Superplastic Nanomolding. *Phys. Rev. Lett.* **2019**, *122*, 016101.
(58) Liu, N.; Xie, Y.; Liu, G.; Sohn, S.; Raj, A.; Han, G.; Wu, B.; Cha, J. J.; Liu, Z.; Schroers, J. General Nanomolding of Ordered Phases. *Phys. Rev. Lett.* **2020**, *124*, 036102.
(59) Kraftmakher, Y. Equilibrium Vacancies and Thermophysical Properties of Metals. *Phys. Rep.* **1998**, *299*, 79−188.


https://doi.org/10.1021/acsnano.1c02636
*ACS Nano* XXXX, XXX, XXX−XXX

(60) Chan, G. H.; Zhao, J.; Hicks, E. M.; Schatz, G. C.; Van Duyne, R. P. Plasmonic Properties of Copper Nanoparticles Fabricated by Nanosphere Lithography. *Nano Lett.* **2007**, *7*, 1947−1952.
(61) Teo, B. K.; Sun, X. H. Silicon-Based Low-Dimensional Nanomaterials and Nanodevices. *Chem. Rev.* **2007**, *107*, 1454−1532.
(62) Meng, F. G.; Liu, H. S.; Liu, L. B.; Jin, Z. P. Thermodynamic Description of the Au-Si-Sn System. *J. Alloys Compd.* **2007**, *431*, 292−297.
(63) Chevalier, P. Y. A. Thermodynamic Evaluation of the Au-Ge and Au-Si Systems. *Thermochim. Acta* **1989**, *141*, 217−226.
(64) Wang, J.; Leinenbach, C.; Roth, M. Thermodynamic Modeling of the Au-Ge-Sn Ternary System. *J. Alloys Compd.* **2009**, *481*, 830−836.
(65) Hiraki, A.; Shimizu, A.; Iwami, M.; Narusawa, T.; Komiya, S. Metallic State of Si in Si-Noble-Metal Vapor-Quenched Alloys Studied by Auger-Electron Spectroscopy. *Appl. Phys. Lett.* **1975**, *26*, 57−60.
(66) Green, A. K.; Bauer, E. Formation, Structure, and Orientation of Gold Silicide on Gold Surfaces. *J. Appl. Phys.* **1976**, *47*, 1284−1291.
(67) Franciosi, A.; Niles, D. W.; Margaritondo, G.; Quaresima, C.; Capozi, M.; Perfetti, P. Au-Si Interface Formation: The Other Side of the Problem. *Phys. Rev. B: Condens. Matter Mater. Phys.* **1985**, *32*, 6917−6919.
(68) Mehrer, H. *Diffusion in Solids: Fundamentals, Methods, Materials, Diffusion-Controlled Processes*, 1st ed.; Springer: Berlin, 2007; pp 405, 300.
(69) Yang, R. Y.; Weng, M. H.; Liang, C. T.; Su, Y. K.; Shy, S. L. Low Temperature Metal Induced Crystallization of Amorphous Silicon by Nano-Gold-Particles. *Jpn. J. Appl. Phys.* **2006**, *45*, L1146−L1148.
(70) Zhang, S. Y.; Wang, X. P.; Chen, Z. W.; Wu, Z. Q.; Jin-Phillipp, N. Y.; Kelsch, M.; Phillipp, F. *In Situ* TEM Study of Fractal Formation in Amorphous Ge/Au Bilayer Films. *Phys. Rev. B: Condens. Matter Mater. Phys.* **1999**, *60*, 5904−5908.
(71) Gupta, D. Grain-Boundary Self-Diffusion in Au by Ar Sputtering Technique. *J. Appl. Phys.* **1973**, *44*, 4455−4458.
(72) Bokhonov, B.; Korchagin, M. *In Situ* Investigation of Stage of the Formation of Eutectic Alloys in Si-Au and Si-Al Systems. *J. Alloys Compd.* **2000**, *312*, 238−250.
(73) Bystrenko, O. V.; Kartuzov, V. V. Contact Melting and the Structure of Binary Eutectic near the Eutectic Point. *J. Alloys Compd.* **2014**, *617*, 124−128.





https://doi.org/10.1021/acsnano.1c02636
*ACS Nano* XXXX, XXX, XXX−XXX